# Topological Dirac semimetal phase in Pd and Pt oxides

Gang Li,[1,2,*] Binghai Yan,[3,4] Zhijun Wang,[5] and Karsten Held[1]

[1]*Institute of Solid State Physics, Vienna University of Technology, A-1040 Vienna, Austria*

[2]*School of Physical Science and Technology, ShanghaiTech University, Shanghai 200031, China*

[3]*Max Planck Institute for Chemical Physics of Solids, 01187 Dresden, Germany*

[4]*Max Planck Institute for the Physics of Complex Systems, 01187 Dresden, Germany*

[5]*Department of Physics, Princeton University, Princeton, New Jersey 08544, USA*

(Received 29 February 2016; revised manuscript received 24 November 2016; published 3 January 2017)

Topological Dirac semimetals (DSMs) exhibit nodal points through which energy bands disperse linearly in three-dimensional (3D) momentum space, a 3D analog of graphene. The first experimentally confirmed DSMs with a pair of Dirac points (DPs), $Na_3Bi$ and $Cd_3As_2$, show topological surface Fermi arc states and exotic magnetotransport properties, boosting the interest in the search for stable and nontoxic DSM materials. Based on density-functional theory and dynamical mean-field theory calculations, we predict a family of palladium and platinum oxides to be robust 3D DSMs with three pairs of Dirac points that are well separated from bulk bands. The Fermi arcs at the surface display a Lifshitz transition upon a continuous change of the chemical potential. Corresponding oxides are already available as high-quality single crystals, an excellent precondition for the verification of our predictions by photoemission and magnetotransport experiments, extending DSMs to the versatile family of transition-metal oxides.

DOI: 10.1103/PhysRevB.95.035102

## I. INTRODUCTION

The Dirac semimetal (DSM) is a new quantum state of matter whose low-energy excitations can be described by massless Dirac fermions with a vanishing density of states at the Fermi level. The prototype of a DSM in two dimensions is graphene [1], whose conduction and valence bands cross linearly at a node called the Dirac point (DP). Electrons and holes are massless at the DPs, which can be effectively viewed as two-dimensional (2D) Dirac fermions at low energies. With the mushrooming development of topological insulators (TIs) [2,3], 1D and 2D Dirac fermions are also realized as topological objects at the edge or surface of TIs, respectively. However, the search for 3D DSMs in bulk materials encounters major difficulties, especially in the presence of strong spin-orbital coupling (SOC). Due to the fact that the conduction and valence bands are spin degenerate, they can hybridize and gap out at the DPs. In just the past few years, we have learned that the 3D DPs can be stabilized when these points are protected by additional symmetry that forbids the interband coupling [4]. The 3D DSM phase discovered in both $Na_3Bi$ [5,6] and $Cd_3As_2$ [7–10] with one pair of DPs belongs to this class.

The Dirac point can split into two Weyl nodes when the band degeneracy is lifted by breaking either time-reversal symmetry (TRS) or inversion symmetry (IS), leading to the Weyl semimetal (WSM) [11]. These Weyl points always come in pairs that carry opposite chiralities (handedness). One of the hallmarks of WSMs is the appearance of the Fermi arc that connects a pair of two Weyl points with opposite chiralities, as found by recent theoretical [12–14] and experimental [15–18] works on the TaAs family. Therefore, the DSM can exhibit double Fermi arcs due to the degeneracy of Weyl points, which has been experimentally observed in $Na_3Bi$ [6,19]. In addition, WSMs and DSMs usually show unconventional magnetotransport properties [20–25], such as the chiral anomaly effect [26,27].

So far all the experimentally discovered 3D DSMs exhibit only one specific type of Fermi arc. Important questions arise, such as whether different forms of Fermi arcs in 3D DSMs can coexist and how they interact with each other [28–30]. Here, we propose a family of palladium and platinum oxides that possesses three pairs of DPs, which demonstrates different types of Fermi arcs in a single system. Many of these compounds are already available in the single-crystal form, which provides an ideal starting point for the systematic study of the novel electronic, thermo, and magnetic properties of Fermi arcs and their interactions. Our work also significantly extends the topological DSMs into the versatile family of transition-metal oxides, which may serve as a robust material playground for the interplay between the 3D DSMs and electronic correlations [31,32].

## II. ELECTRONIC STRUCTURE AND TOPOLOGICAL NATURE

Here we investigate theoretically one of the most widely studied phases of noble-metal oxides, $AB_3O_4$ ($A$ = Li, K, Na, Mg, Ca, Sr, Ba, Zn, and Cd; $B$ = Pd and Pt) with space group $Pm\bar{3}n$ (No. 223), as shown in Fig. 1(a). The palladium/platinum atoms at the corner of the cubic cell are located between four coplanar oxygen ions, forming corner-sharing $PdO_4$ and $PtO_4$ tetragons. We calculate the electronic structure of Pd (Pt) $AB_3O_4$ with SOC density-functional theory (DFT). Specifically, we use the full-potential linearized augmented plane-wave method [33,34] with the modified Becke-Johnson exchange potential [35] to account for the correlation effect. The calculations are further confirmed by employing DFT+U and DFT+ dynamical mean-field theory [36–38] (DMFT) functionals. We use $K_{\max}\mathrm{RMT} = 9.0$ and a $10 \times 10 \times 10$ $k$-mesh for the ground-state calculations,

*Author to whom all correspondence should be addressed: gangli.phy@gmail.com

 

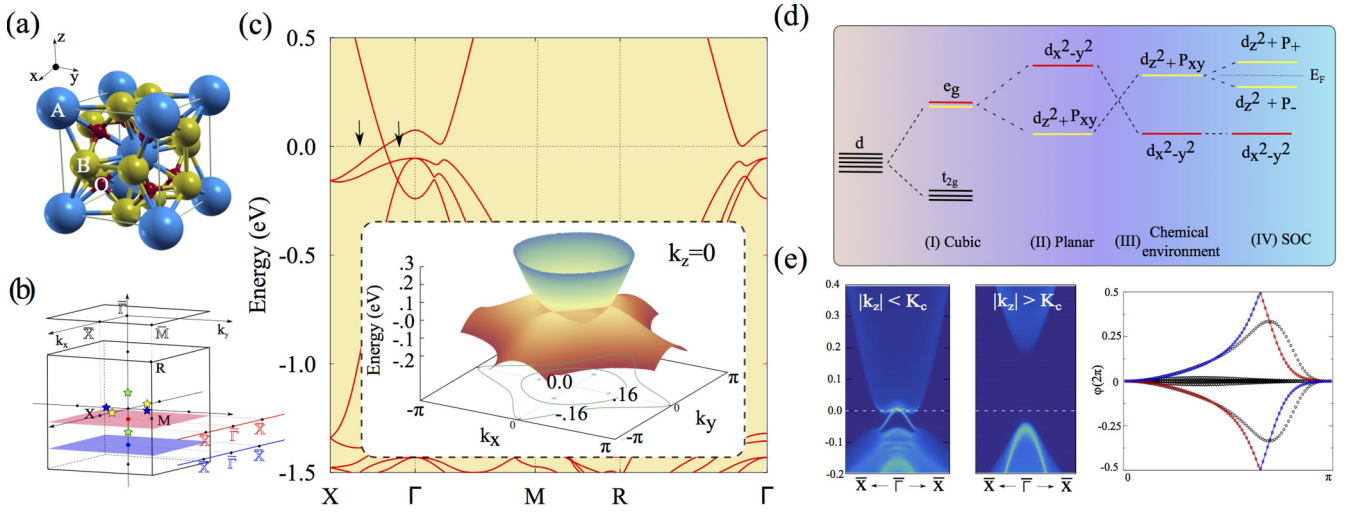


FIG. 1. Electronic structure of $AB_3O_4$. (a) Crystal structure of $AB_3O_4$, which contains $A$ atoms (blue) at the corner and $B$ atoms (beige) on each surface, which are surrounded by four coplanar oxygen ions (red). (b) First Brillouin zone with the three pairs of DPs (colored stars). The pink and light blue plane are 2D cuts of the 3D BZ with $|k_z| < k_z^c$ (pink) and $|k_z| > k_z^c$ (light blue). These two $k_z$ values are indicated by arrows in (c). (c) Electronic structure of prototypical $SrPd_3O_4$. Between $X$ and $\Gamma$, the conduction and valence bands cross linearly at the Fermi level, featuring a 3D DP. There are in total three pairs of DPs located at the $k_x$, $k_y$, and $k_z$ axes. The inset shows the highest valence band and the lowest conduction bands, which touch at four DPs in the $k_z = 0$ plane. (d) The DPs are induced by a band inversion at $\Gamma$ formed by the Pd (Pt) $e_g$ orbital and its hybridization with the $p$ orbital of the oxygen atoms. (e) The topological nature is characterized by the Wilson loop spectrum around the DPs and the different edges states at the two 2D planes shown in (b). Topological edge states are found at the edge of a plane with $|k_z| < k_z^c$, while they are missing at the edge of a plane with $|k_z| > k_z^c$.

where RMT represents the smallest muffin-tin radius and $K_{\max}$ is the maximum size of reciprocal-lattice vectors. The surface electronic structures are further calculated using the maximally localized Wannier functions (MLWFs) [39] employing the WIEN2WANNIER [40] interface.

Figure 1(c) displays the electronic structure of $SrPd_3O_4$ with the corresponding 3D Brillouin zone (BZ) shown in Fig. 1(b). As can be clearly seen, there is a linear band crossing, i.e., a DP, at the Fermi level between $X$ and $\Gamma$, featuring the system a Dirac semimetal. There are six equivalent $X$ points in these systems, and the DPs between $X$ and $\Gamma$ thus form three pairs located at $k_x$, $k_y$, and $k_z$ axes, respectively. This is similar to the cases of $Cu_3NX$, with $X = \{$Ni, Cu, Pd, An, Ag, Cd$\}$ [41–43], where the three pairs of DPs are located around the $R$ point instead with the Fermi surfaces less well separated from the bulk bands. As we will see later on, the DPs in our compounds also display completely different topological surface states. In the inset of Fig. 1(c), a 3D plot of the highest valence and the lowest conduction bands for the $k_z = 0$ plane is shown, where the two pairs of DPs at the $k_x$ and $k_y$ axes can be clearly seen.

We find that, in addition to the TRS and IS, these DPs are protected by the fourfold screw rotation symmetry $\tilde{C}_4$ [4,28,44,45]. These screw axes are simply the Pd-Pd (Pt-Pt) chain at each surface of the crystal. Due to the protection from the screw axes symmetries, the DPs in palladium (platinum) oxides $AB_3O_4$ are stable against disorders. Strain applied to the $z$ direction breaks the screw axes symmetry at the $x$ and $y$ directions, and an energy gap at the $k_{xy}$ plane can then be opened (not shown), leaving the system with only a single pair of DPs at the $k_z$ axis. It is also possible in principle to trigger a phase transition from DSM to strong TI by gaping out the DPs at all three axes.

Furthermore, we find that the DSM phase discovered in $AB_3O_4$ is topologically nontrivial, which is manifested by the Pd (Pt) $d_{x^2-y^2}$ and $d_{z^2}$ band inversion at $\Gamma$ as shown in Fig. 1(d). The inverted band structure leads to another marvellous phenomenon in these topological DSMs—the appearance of topological edge states (TESs) at the edge of a 2D cut of the 3D BZ [46]. This serves as additional independent proof for the topological nature of these systems. In Fig. 1(b), two 2D cuts at different $k_z$ are shown as examples. When $|k_z| < k_z^c$, the $d_{x^2-y^2}$ and $d_{z^2}$ bands are inverted, while when $|k_z| > k_z^c$ they are not. Thus, the two different 2D cuts carry different 2D topological indices. TESs are supposed to appear along the edges of planes with $|k_z| < k_z^c$. By using the recursive Green's-function approach [47], we indeed found TESs connecting the valence and conduction bands at the plane with $|k_z| < k_z^c$, while for $|k_z| > k_z^c$ the system is a trivial insulator with a band gap; see Fig. 1(e). Similar behavior holds for the DPs at the $k_x$ and $k_y$ axes as well.

We further confirm the topological nature of the proposed compounds by calculating the Wilson loop spectrum [48] on a spherical surface enclosing a Dirac point, e.g., $(0, 0, k_z^c)$. We plot the phase $\varphi_i$ of the individual Wilson loop eigenvalues $e^{i\varphi_i}$ as a function of the azimuthal angle $\theta$. On a given-$\theta$ Wilson loop, $(r\sin(\theta)\cos(\phi), r\sin(\theta)\sin(\phi), k_z(\theta))$ with $k_z(\theta) = k_z^c + r\cos(\theta)$ and the spherical radius $r$, the Wilson loop is mapped as $\tilde{C}_{4z} W_{2\pi\leftarrow 0} \tilde{C}_{4z}^{-1} = W_{\frac{5\pi}{2}\leftarrow\frac{\pi}{2}} = W_{\frac{\pi}{2}\leftarrow 0} W_{2\pi\leftarrow 0} W_{0\leftarrow\frac{\pi}{2}}$, where $W_{B\leftarrow A}$ represents a parallel transport from $\phi = A$ to $B$. After redefining a symmetry $\mathcal{C}_{4z} \equiv W_{\frac{\pi}{2}}^{-1} \tilde{C}_{4z}$ that satisfies $\mathcal{C}_{4z} W_{2\pi\leftarrow 0} \mathcal{C}_{4z}^{-1} = W_{2\pi\leftarrow 0}$, each Wilson energy $\varphi_i$

can be labeled by $\lambda_\alpha e^{i[k_z(\theta)/2+\varphi_i/4]}$ with $\lambda_i = e^{i(2n-1)\pi/4}$ for $i \in \{1,2,3,4\}$, where we further use $\mathcal{C}^4_{4z} = W^{-1}_{2\pi\leftarrow 0}\tilde{C}^4_{4z} = -e^{-i\varphi_i}\, e^{-2ik_z(\theta)}$. As shown in the rightmost plot of Fig. 1(e), the two Wilson eigenstates colored in blue and red belong to different eigenstates, which do not hybridize. They clearly indicate two hidden Berry curvature fluxes, one with Chern number +1 and the other with Chern number −1. The difference of the two individual Chern numbers mod 2 constitutes a $\mathcal{Z}_2$ topological invariant for the Dirac point.

The above-mentioned two inverted bands are described by $\Gamma_6^-$ and $\Gamma_7^-$ irreducible representations. Under the TRS, IS, and $\tilde{C}_4$ symmetries, an effective Hamiltonian can be constructed at Γ,

$$H(\vec{k}) = \epsilon_0(\vec{k}) + \begin{pmatrix} M(\vec{k}) & S \\ S^\dagger & -M(\vec{k}), \end{pmatrix} \tag{1}$$

where $\epsilon_0(\vec{k}) = D + E\vec{k}^2$, $M(\vec{k}) = B - C\vec{k}^2$, and $S = iA(k_x k_y \sigma_z + k_y k_z \sigma_x + k_z k_x \sigma_y)$ with $\vec{k}^2 = k_x^2 + k_y^2 + k_z^2$ and $\sigma_{x,y,z}$ Pauli matrices. $A, B, C, D, E$ are model parameters that one can obtain by fitting this Hamiltonian with the corresponding electronic structures of different compounds, e.g., $SrPd_3O_4$ in Fig. 1. Diagonalizing this Hamiltonian leads to the dispersion $E(\vec{k}) = \epsilon_0(\vec{k}) \pm \sqrt{M(\vec{k})^2 + A^2(k_x^2k_y^2 + k_y^2k_z^2 + k_z^2k_x^2)}$, from which we immediately see that there is one pair of DPs on each axis at $k_c = \pm\sqrt{B/C}$, which is consistent with the *ab initio* calculations.

## III. FERMI ARCS AND LIFSHITZ TRANSITION

Topological DSMs host nontrivial open Fermi surfaces connecting opposite chiral charges. In the Pd and Pt oxides proposed in this work, we discover multiple pairs of DPs. Each DP can be viewed as two copies of Weyl nodes with opposite chiral charges. Fermi arcs may appear and connect one positive Weyl node with one negative Weyl node. In principle, any positive Weyl node can be connected to any other negative Weyl node in the system. Therefore, the question of how the opposite chiral charges among these DPs are connected by Fermi arcs naturally arises. Here, we choose the (001) surface to answer this question, and we demonstrate that two different types of Fermi arcs coexist in these systems, which has not been reported before in the literature.

Before discussing the detailed Fermi arc pattern, we provide a simple argument on the possible constraints. For the Pd and Pt oxides $AB_3O_4$, the (001) surface remains unchanged under the $C_2$ rotational symmetry and mirror symmetry, i.e., $(x,y,z) \xrightarrow{C_2} (-x,-y,z)$, $(x,y,z) \xrightarrow{M_x} (-x,y,z)$, $(x,y,z) \xrightarrow{M_y} (x,-y,z)$. In momentum space, the two DPs along the $k_z$ axis project to the same surface $\overline{\Gamma}$ point, while only the other two pairs of DPs located at the $k_x$ and $k_y$ axes remain separated on the (001) surface. The Hamiltonian of the Fermi arcs $H_{\rm arc}$ for these two pairs of DPs transforms under these two symmetries as $C_2 H_{\rm arc}(k_x,k_y,k_z)C_2^{-1} = H_{\rm arc}(-k_x,-k_y,k_z)$, $M_x H_{\rm arc}(k_x,k_y,k_z)M_x^{-1} = H(-k_x,k_y,k_z)$, and $M_y H_{\rm arc}(k_x,k_y,k_z)M_y^{-1} = H_{\rm arc}(k_x,-k_y,k_z)$. Together with the necessity that a Weyl node with negative chirality connects to a Weyl node with positive chirality, this allows us to identify the four possible types of Fermi arcs illustrated in Figs. 2(a)–2(d). Here, the Fermi arcs with the same color transform onto each other under $C_2$ and mirror symmetry. In Fig. 2(a), the two DPs along the same axis are connected by two Fermi arcs. These are the ordinary Fermi arcs observed also in $Na_3Bi$ [6,19]. But since we have more than one pair of DPs, the intersection of two ordinary Fermi arcs can hybridize and deform into the other types.

This is confirmed by our direct calculation of the surface states shown in Fig. 2(e), which implies that the Pd and Pt oxides $AB_3O_4$ host the Fermi arcs shown in Figs. 2(c) and 2(d). In the middle panel of Fig. 2(e), we plot the topological surface states along two high-symmetry paths $\overline{\Gamma} \to \overline{X}$ and $\overline{\Gamma} \to \overline{M}$. The bands with stronger intensity (red) are at the surface, while the shadow bands in the background are of bulk character. The bulk valence and conduction bands touch at the nodal point between $\overline{\Gamma}$ and $\overline{X}$, featuring the 3D DPs at the $k_x$ and $k_y$ axes. As is clearly shown, there are topological surface states connecting the bulk valence and conduction bands and they behave differently along the two chosen high-symmetry paths.

On the left- and right-hand sides of Fig. 2(e), plots of Fermi arcs in the entire 2D surface BZ at eight chosen binding energies are shown. As the axis of the bulk Dirac cone is tilted, its intersection with the constant energy plane displays an elliptic shape, which is indicated in yellow in these plots. At the Fermi level, Fermi arcs display a Fig. 2(c)–type pattern. This corresponds to the same type of Fermi arcs observed already in $Na_3Bi$. On top of this we observe, however, additional Fermi surface around the DPs at the $k_x$ axis connecting the two opposite chiral charges from the same DP. These two Fermi surfaces are symmetric with respect to the surface $\overline{\Gamma}$ point and $k_y$ axis. Let us emphasize that these are different Fermi arcs as compared to the ones parallel to the $k_y$ axis. They are isoenergy projections of the Riemann surface states recently proposed in Ref. [30], which distinguishes these from the ordinary Fermi arcs, as the latter stay always separated in the surface BZ. Continuously decreasing the chemical potential significantly modifies the Fermi surfaces connecting the opposite chiral charges at each DP at the $k_x$ axis, while the Fermi arcs connecting the two DPs at the $k_y$ axis remains topologically unchanged.

We note that the shrinking of the Fermi arcs results from the intersection of the helicoid and the antihelicoid Riemann surfaces along the $k_x$ axis at the Dirac cone. The intersection of them always appears at the $k_x$ axis, which is required by the $C_2$ rotational symmetry and mirror symmetry preserved on this surface. Unlike WSMs, the Fermi arcs in 3D DSMs are not stable against symmetry-allowed perturbations. They can be continuously deformed into other forms without breaking any symmetry [28–30]. Indeed, by further decreasing energy, we observe a Lifshitz transition of the Fermi surface, which is shown on the right-hand side of Fig. 1(e). Here, two types of Fermi arcs now merge into one single type of Fermi arc shown in Fig. 1(d), e.g., the opposite chiral charges located at $k_x^c$ and $k_y^c$ are now connected by one open Fermi surface. Under $C_2$ rotation and mirror symmetries, altogether four copies of it show up in the entire 2D surface BZ forming a diamond shape structure. Note that the detailed shape of the Fermi arcs in these compounds depends on the surface termination and reconstructions; in reality, the latter may modify the shape of the Fermi arcs discussed in this paper. However, the Dirac SM

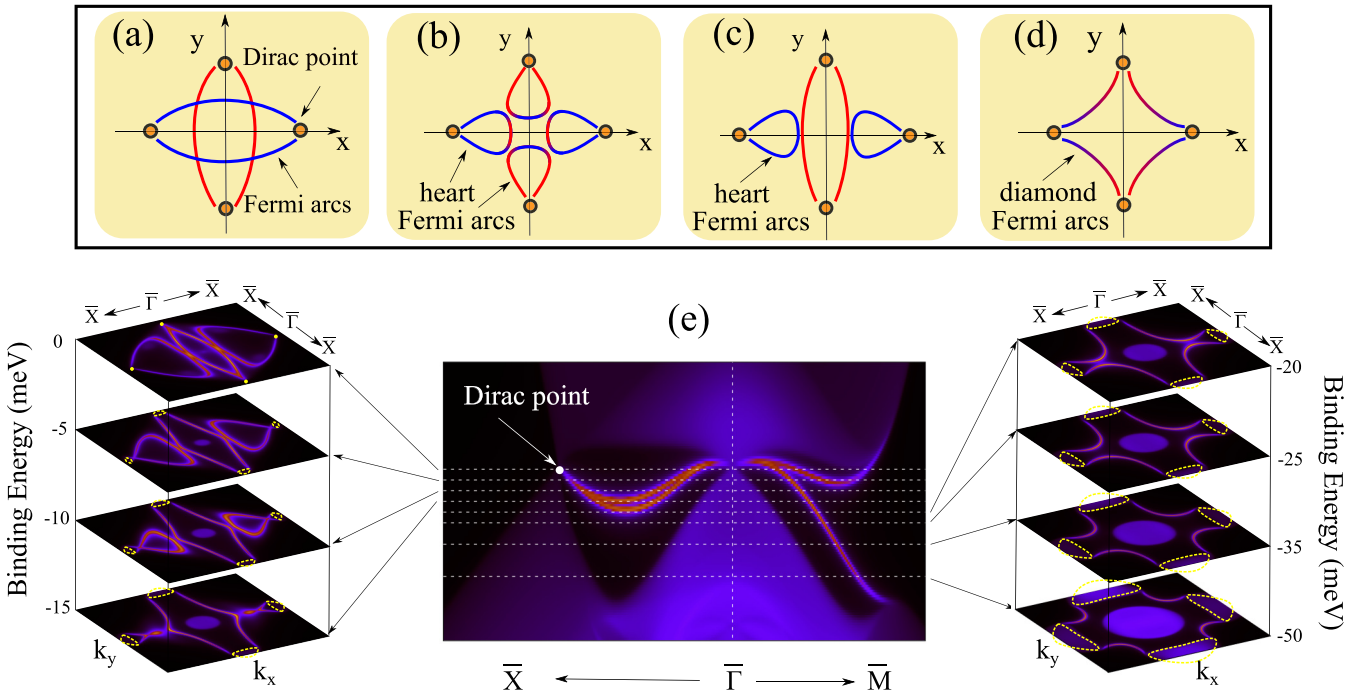


FIG. 2. "Double Fermi arcs" of noble-metal oxides $AB_3O_4$. (a)–(d) Four symmetry-allowed Fermi arcs on the (001) surface connecting the opposite chiral charges at the DPs, which can display both heart and diamond shapes. (e) The topological surface states on the (001) surface are shown along two high-symmetry paths [see Fig. 1(b) for the BZ]. Below the Fermi level, eight different constant energy cuts are taken to illustrate the Fermi arcs in the entire surface BZ and their evolution. The evolution for the bulk DPs at the Fermi level to a cone at finite binding energies is indicated by closed yellow circles.

nature of the proposed compounds is always free of surface effects as it is fully determined by the corresponding bulk property. Hence there should always be topological states connecting different DPs. Since these DPs are all at the Fermi level, as long as these topological states are not masked by the bulk states (as observed in our calculations), changing the energy level results in a continuous change of the Fermi surface shape due to the curvature of these topological states.

## IV. ELECTRONIC CORRELATIONS

Before closing, we want to further comment on the possible influence of electronic correlations in these compounds. The 4*d* and 5*d* compounds proposed in this work are subject to electronic correlations. It is known that conventional DFT calculations usually fail for correlated systems. To amend this problem, we have applied the mBJ exchange potential in our calculations. Here we further provide affirmative evidence on the Dirac semimetal nature of these compounds in Fig. 3. We determined the bulk electronic structure of $SrPd_3O_4$ also from DFT+U [Fig. 3(a)] and more sophisticated DFT+DMFT [Fig. 3(b)] calculations. For the latter, we used the embedded-DMFT [49] (version 2015) with density-density interaction at inverse temperature $\beta t = 50$ and projector 4. In both calculations, $U = 3.76$ and $J = 0.8$ are used for Pd *d* orbitals as obtained from a cRPA calculation [50]. Despite the spectra broadening from the self-energy and the slight modifications in the high-energy sector in the DFT+DMFT, both methods consistently confirm the conclusion shown in Fig. 1 that the correlated compound $SrPd_3O_4$ is a Dirac SM. This is not surprising as the DPs in these system are protected by TR and the rotational symmetries. As long as they are not broken by interactions, the semimetal phase as well as the associated Lifshitz transition will survive. To prove the latter, we further show the bulk DPs and the topological surface states calculated with the DFT+U functional in Fig. 3(c), which are

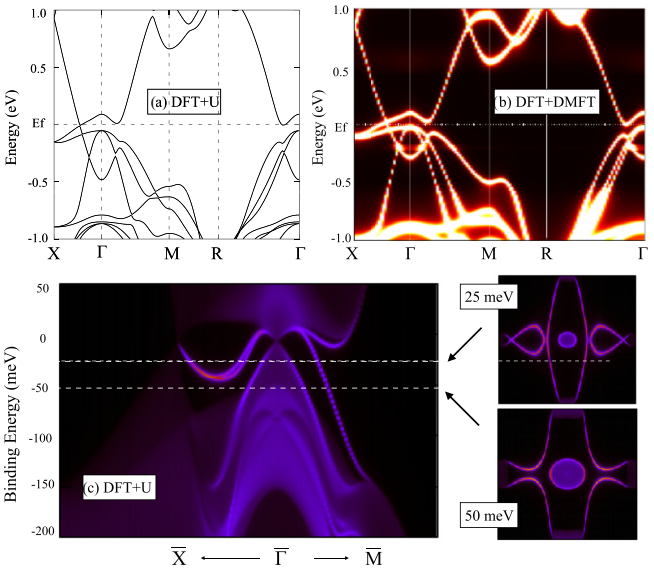


FIG. 3. Bulk electronic structure of $SrPd_3O_4$ from (a) DFT+U and (b) DFT+DMFT calculations with SOC. (c) The topological surface states calculated from the DFT+U functional.

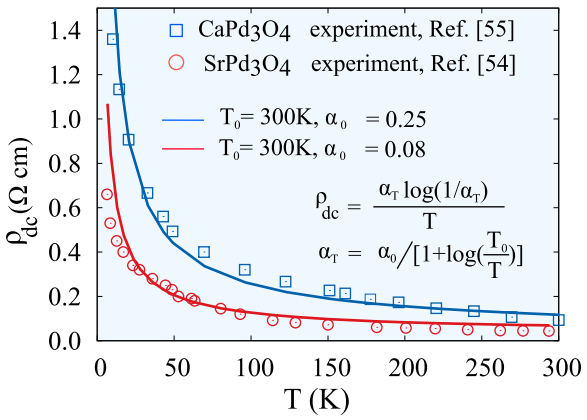


FIG. 4. Resistivity anomaly in correlated semimetals. The small residual resistivity at $T \to 0$ and the temperature dependence of the resistivity in $SrPd_3O_4$ and $CaPd_3O_4$ can be explained by a DSM with long-range Coulomb interaction; see Refs. [51,52].

similar to those in Fig. 2 from DFT+mBJ calculations. The detailed curvature of the topological surface states is modified, while the Lifshitz transition is still present upon changing the binding energies; see Fig. 3(c).

Another appealing feature of electronic correlations in transition-metal oxide (TMO) DSMs is that, as is known, the long-range Coulomb interaction can relax the transportation of electrons, leading to a logarithmic correction to their linear resistivity in semimetals, which may explain the transport anomaly observed in $SrPd_3O_4$ and $CaPd_3O_4$. The resistivity of $SrPd_3O_4$ and $CaPd_3O_4$ remains finite for $T \to 0$ and decreases with increasing temperature (shown as symbols in Fig. 4). This is clearly different from the experimentally confirmed DSMs, i.e., $Cd_3As_2$ and $Na_3Bi$, which display a clear metallic behavior with a tiny resistivity at zero temperature [20,53]. The resistivity in $SrPd_3O_4$ and $CaPd_3O_4$ at $T \to 0$ is four to five orders of magnitude smaller than typical values for semiconductors: it is $\sim 10^{-3}$ $\Omega$ m in $SrPd_3O_4$ [54] and $CaPd_3O_4$ [55,56]. Previously, this has been interpreted as a semiconductor with a tiny energy gap. We note, however, that a similar resistivity anomaly was also observed in the topological Weyl SM $Y_2Ir_2O_7$ [57], which is $\sim 3 \times 10^{-2}$ $\Omega$ m at zero temperature and also decreases with increasing temperature. Both the residue and the temperature dependence of the resistivity in $SrPd_3O_4$ and $CaPd_3O_4$ resemble strongly those of $Y_2Ir_2O_7$. For the topological SM $Y_2Ir_2O_7$, it was found that the Coulomb interaction can relax the conductivity of electrons [52], which successfully explains the low-temperature resistivity anomaly of this compound. We find that the experimental data of $SrPd_3O_4$ and $CaPd_3O_4$ can also be fitted by a similar resistivity expression [51]; see the lines in Fig. 4. If this mechanism is confirmed, the emergence of a Dirac semimetal phase in TMO will provide a beautiful platform for studying novel transport properties of topological materials in the presence of electronic correlations.

## V. CONCLUSION

In conclusion, our systematic study regarding the electronic structure of palladium and platinum oxides $AB_3O_4$ with space group $Pm\bar{3}n$ establishes this family of materials to be the first TMO family that hosts multiple pairs of DPs in one system. The coexistence of different forms of Fermi arcs further distinguishes them from other DSMs discovered so far. We observe Fermi arcs of different shapes, as well as a Lifshitz transition between them. This Lifshitz transition occurs upon changing the binding energy in our calculations, but as a matter of course it can be equivalently triggered by changing the chemical potential. Experimentally this is feasible by a gate electrode or doping the systems. Hence we have a material where the topological properties can be tuned dramatically. This in turn affects, e.g., quantum oscillation measurements. Due to the availability of clean single crystals, the rich and striking features of this family of materials makes it an ideal platform to experimentally study multiple DPs and the interaction of their open Fermi surfaces. Our theoretical proposal provides an ideal playground for studying the interplay between electronic correlation and nontrivial topology in 3D Dirac SMs. It also paves the way for a future experimental study of the electronic, transport, and spectroscopic properties.

## ACKNOWLEDGMENTS

We acknowledge financial support by the European Research Council under the European Union's Seventh Framework Program (FP/2007-2013)/ERC through Grant Agreement No. 306447 and the Austrian Science Fund (FWF) through project ID I 1395-N26 as part of the DFG research unit FOR 1346 (G.L. and K.H.). Calculations have been done in part on the Vienna Scientific Cluster (VSC).

TABLE I. Lattice parameters $a$ (in Å) and DP position (in meV) relative to the Fermi level for various palladium and platinum oxides.

| $A$ | Pd ($a$, Å) | Pd (DP, meV) | Pt ($a$, Å) | Pt (DP, meV) |
|---|---|---|---|---|
| Li | × | × | 5.634 [58] | 227 |
| K | × | × | 5.679 [58] | 225 |
| Na | 5.655 [58], 5.650 [59] | 202 | 5.670 [58,60], 5.687 [61] | 281 |
| Mg | × | × | 5.640 [58] | 10 |
| Ca | 5.747 [58], 5.747 [62] | 44 | 5.743 [58] | 45 |
| Sr | 5.825 [58], 5.822 [54], 5.826 [62] | 0.0 | × | × |
| Ba | × | × | 5.715 [58] | 11 |
| Zn | × | × | 5.649 [58] | 52 |
| Cd | 5.740 [55,58], 5.742 [62] | 0.0 | 5.687 [58] | 0.0 |

## APPENDIX: LATTICE PARAMETER, BINDING ENERGY OF DPs, AND ELECTRONIC STRUCTURE

Supplementarily, we provide in Table I the lattice parameters for all the compounds studied in our paper, which are reported in the literature. From DFT+mBJ calculations, we found that not all compounds have their DPs exactly at the Fermi level. We thus present the offsets of their locations with respect to the Fermi level in the table as well. For systems with DPs above the Fermi level, the topological surface states still extend down to the valence bands [see Fig. 2(e)], which can be observed in, for example, angle-resolved photoemission spectroscopy.


[1] A. H. Castro Neto, F. Guinea, N. M. R. Peres, K. S. Novoselov, and A. K. Geim, Rev. Mod. Phys. **81**, 109 (2009).
[2] M. Z. Hasan and C. L. Kane, Rev. Mod. Phys. **82**, 3045 (2010).
[3] X.-L. Qi and S.-C. Zhang, Rev. Mod. Phys. **83**, 1057 (2011).
[4] B.-J. Yang and N. Nagaosa, Nat. Commun. **5**, 4898 (2014).
[5] Z. Wang, Y. Sun, X.-Q. Chen, C. Franchini, G. Xu, H. Weng, X. Dai, and Z. Fang, Phys. Rev. B **85**, 195320 (2012).
[6] Z. K. Liu, B. Zhou, Y. Zhang, Z. J. Wang, H. M. Weng, D. Prabhakaran, S.-K. Mo, Z. X. Shen, Z. Fang, X. Dai, Z. Hussain, and Y. L. Chen, Science **343**, 864 (2014).
[7] Z. Wang, H. Weng, Q. Wu, X. Dai, and Z. Fang, Phys. Rev. B **88**, 125427 (2013).
[8] S. Borisenko, Q. Gibson, D. Evtushinsky, V. Zabolotnyy, B. Büchner, and R. J. Cava, Phys. Rev. Lett. **113**, 027603 (2014).
[9] M. Neupane, S.-Y. Xu, R. Sankar, N. Alidoust, G. Bian, C. Liu, I. Belopolski, T.-R. Chang, H.-T. Jeng, H. Lin, A. Bansil, F. Chou, and M. Z. Hasan, Nat. Commun. **5**, 3786 (2014).
[10] Z. K. Liu, J. Jiang, B. Zhou, Z. J. Wang, Y. Zhang, H. M. Weng, D. Prabhakaran, S.-K. Mo, H. Peng, P. Dudin, T. Kim, M. Hoesch, Z. Fang, X. Dai, Z. X. Shen, D. L. Feng, Z. Hussain, and Y. L. Chen, Nat. Mater. **13**, 677 (2014).
[11] X. G. Wan, A. M. Turner, A. Vishwanath, and S. Y. Savrasov, Phys. Rev. B **83**, 205101 (2011).
[12] H. Weng, C. Fang, Z. Fang, B. A. Bernevig, and X. Dai, Phys. Rev. X **5**, 011029 (2015).
[13] S.-M. Huang, S.-Y. Xu, I. Belopolski, C.-C. Lee, G. Chang, B. Wang, N. Alidoust, G. Bian, M. Neupane, C. Zhang, S. Jia, A. Bansil, H. Lin, and M. Z. Hasan, Nat. Commun. **6**, 7373 (2015).
[14] Y. Sun, S. C. Wu, and B. Yan, Phys. Rev. B **92**, 115428 (2015).
[15] B. Q. Lv, H. M. Weng, B. B. Fu, X. P. Wang, H. Miao, J. Ma, P. Richard, X. C. Huang, L. X. Zhao, G. F. Chen, Z. Fang, X. Dai, T. Qian, and H. Ding, Phys. Rev. X **5**, 031013 (2015).
[16] S.-Y. Xu, I. Belopolski, N. Alidoust, M. Neupane, G. Bian, C. Zhang, R. Sankar, G. Chang, Z. Yuan, C.-C. Lee, S.-M. Huang, H. Zheng, J. Ma, D. S. Sanchez, B. Wang, A. Bansil, F. Chou, P. P. Shibayev, H. Lin, S. Jia, and M. Z. Hasan, Science **349**, 613 (2015).
[17] L. X. Yang, Z. K. Liu, Y. Sun, H. Peng, H. F. Yang, T. Zhang, B. Zhou, Y. Zhang, Y. F. Guo, M. Rahn, P. Dharmalingam, Z. Hussain, S. K. Mo, C. Felser, B. Yan, and Y. L. Chen, Nat. Phys. **11**, 728 (2015).
[18] Z. K. Liu, L. X. Yang, Y. Sun, T. Zhang, H. Peng, H. F. Yang, C. Chen, Y. Zhang, Y. F. Guo, D. Prabhakaran, M. Schmidt, Z. Hussain, S. K. Mo, C. Felser, B. Yan, and Y. L. Chen, Nat. Mater. **15**, 27 (2016).
[19] S.-Y. Xu, C. Liu, S. K. Kushwaha, R. Sankar, J. W. Krizan, I. Belopolski, M. Neupane, G. Bian, N. Alidoust, T.-R. Chang, H.-T. Jeng, C.-Y. Huang, W.-F. Tsai, H. Lin, P. P. Shibayev, F.-C. Chou, R. J. Cava, and M. Z. Hasan, Science **347**, 294 (2015).
[20] T. Liang, Q. Gibson, M. N. Ali, M. Liu, R. J. Cava, and N. P. Ong, Nat. Mater. **14**, 280 (2014).
[21] A. Narayanan, M. D. Watson, S. F. Blake, N. Bruyant, L. Drigo, Y. L. Chen, D. Prabhakaran, B. Yan, C. Felser, T. Kong, P. C. Canfield, and A. I. Coldea, Phys. Rev. Lett. **114**, 117201 (2015).
[22] C. Shekhar, A. K. Nayak, Y. Sun, M. Schmidt, M. Nicklas, I. Leermakers, U. Zeitler, W. Schnelle, J. Grin, C. Felser, and B. Yan, Nat. Phys. **11**, 645 (2015).
[23] X. Huang, L. Zhao, Y. Long, P. Wang, D. Chen, Z. Yang, H. Liang, M. Xue, H. Weng, Z. Fang, X. Dai, and G. Chen, Phys. Rev. X **5**, 031023 (2015).
[24] C. Zhang, S.-Y. Xu, I. Belopolski, Z. Yuan, Z. Lin, B. Tong, N. Alidoust, C.-C. Lee, S.-M. Huang, H. Lin, M. Neupane, D. S. Sanchez, H. Zheng, G. Bian, J. Wang, C. Zhang, T. Neupert, M. Zahid Hasan, and S. Jia, arXiv:1503.02630.
[25] J. Xiong, S. K. Kushwaha, T. Liang, J. W. Krizan, M. Hirschberger, W. Wang, R. J. Cava, and N. P. Ong, Science **350**, 413 (2015).
[26] S. L. Adler, Phys. Rev. **177**, 2426 (1969).
[27] J. S. Bell and R. Jackiw, Nuovo Cimento A **60**, 47 (1969).
[28] C.-K. Chiu and A. P. Schnyder, Phys. Rev. B **90**, 205136 (2014).
[29] M. Kargarian, M. Randeria, and Y.-M. Lu, Proc. Natl. Acad. Sci. USA **113**, 8648 (2016).
[30] C. Fang, L. Lu, J. Liu, and L. Fu, Nat. Phys. **12**, 936 (2016).
[31] A. Sekine and K. Nomura, Phys. Rev. B **90**, 075137 (2014).
[32] G. Li, W. Hanke, G. Sangiovanni, and B. Trauzettel, Phys. Rev. B **92**, 235149 (2015).
[33] D. J. Singh and L. Nordstrom, *Planewaves, Pseudopotentials, and the LAPW Method*, 2nd ed. (Kluwer Academic, Boston, 2006).
[34] P. Blaha, K. Schwarz, G. Madsen, D. Kvasnicka, and J. Luitz, *WIEN2K, An Augmented Plane Wave + Local Orbitals Program for Calculating Crystal Properties* (Karlheinz Schwarz, Tech. Universitat Wien, Austria, 2001).
[35] F. Tran and P. Blaha, Phys. Rev. Lett. **102**, 226401 (2009).
[36] K. Held, Adv. Phys. **56**, 829 (2007).
[37] A. Georges, G. Kotliar, W. Krauth, and M. J. Rozenberg, Rev. Mod. Phys. **68**, 13 (1996).
[38] G. Kotliar, S. Y. Savrasov, K. Haule, V. S. Oudovenko, O. Parcollet, and C. A. Marianetti, Rev. Mod. Phys. **78**, 865 (2006).
[39] A. A. Mostofi, J. R. Yates, Y.-S. Lee, I. Souza, D. Vanderbilt, and N. Marzari, Comput. Phys. Commun. **178**, 685 (2008).
[40] J. Kuneš, R. Arita, P. Wissgott, A. Toschi, H. Ikeda, and K. Held, Comput. Phys. Commun. **181**, 1888 (2010).
[41] L. S. Xie, L. M. Schoop, E. M. Seibel, Q. D. Gibson, W. Xie, and R. J. Cava, APL Mater. **3**, 083602 (2015).
[42] Y. Kim, B. J. Wieder, C. L. Kane, and A. M. Rappe, Phys. Rev. Lett. **115**, 036806 (2015).

[43] R. Yu, H. Weng, Z. Fang, X. Dai, and X. Hu, Phys. Rev. Lett. **115**, 036807 (2015).
[44] S. M. Young, S. Zaheer, J. C. Y. Teo, C. L. Kane, E. J. Mele, and A. M. Rappe, Phys. Rev. Lett. **108**, 140405 (2012).
[45] Z. Gao, M. Hua, H. Zhang, and X. Zhang, Phys. Rev. B **93**, 205109 (2016).
[46] T. Morimoto and A. Furusaki, Phys. Rev. B **89**, 235127 (2014).
[47] M. P. L. Sancho, J. M. L. Sancho, J. M. L. Sancho, and J. Rubio, J. Phys. F **15**, 851 (1985).
[48] R. Yu, X. L. Qi, A. Bernevig, Z. Fang, and X. Dai, Phys. Rev. B **84**, 075119 (2011).
[49] http://hauleweb.rutgers.edu.
[50] E. Şaşıoğlu, C. Friedrich, and S. Blügel, Phys. Rev. B **83**, 121101 (2011).
[51] P. Goswami and S. Chakravarty, Phys. Rev. Lett. **107**, 196803 (2011).
[52] P. Hosur, S. A. Parameswaran, and A. Vishwanath, Phys. Rev. Lett. **108**, 046602 (2012).
[53] S. K. Kushwaha, J. W. Krizan, B. E. Feldman, A. Gyenis, M. T. Randeria, J. Xiong, S.-Y. Xu, N. Alidoust, I. Belopolski, T. Liang, M. Zahid Hasan, N. P. Ong, A. Yazdani, and R. J. Cava, APL Mater. **3**, 041504 (2015).
[54] T. C. Ozawa, A. Matsushita, Y. Hidaka, T. Taniguchi, S. Mizusaki, Y. Nagata, Y. Noro, and H. Samata, J. Alloys Compd. **448**, 77 (2008).
[55] H. Samata, S. Tanaka, S. Mizusaki, Y. Nagata, T. Ozawa, A. Sato, and K. Kosuda, J. Cryst. Proc. Technol. **2**, 16 (2012).
[56] S. Ichikawa and I. Terasaki, Phys. Rev. B **68**, 233101 (2003).
[57] D. Yanagishima and Y. Maeno, J. Phys. Soc. Jpn. **70**, 2880 (2001).
[58] L. V. B. and S. I. S., J. Inorg. Chem. (translated from Zh. Neorg. Khim.) **23**, 1610 (1978).
[59] R. V. Panin, N. R. Khasanova, A. M. Abakumov, E. V. Antipov, G. Van Tendeloo, and W. Schnelle, J. Solid State Chem. **180**, 1566 (2007).
[60] C. L. McDaniel, J. Solid State Chem. **9** 139 (1974).
[61] K. B. Schwartz, C. T. Prewitt, R. D. Shannon, L. M. Corliss, J. M. Hastings, and B. L. Chamberland, Acta Crystallogr. Sect. B **38**, 363 (1982).
[62] O. Muller and R. Roy, Advances in Chemistry **98**, 28 (1971).